

Scalable and highly selective graphene-based ion-exchange membranes with tunable permselectivity

Original

Scalable and highly selective graphene-based ion-exchange membranes with tunable permselectivity / AIXALA PERELLO, Anna; Pedico, Alessandro; Laurenti, Marco; Fontananova, Enrica; Bocchini, Sergio; Vito Ferrari, Ivan; Lamberti, Andrea. - In: NPJ 2D MATERIALS AND APPLICATIONS. - ISSN 2397-7132. - 7:1(2023), pp. 1-12. [10.1038/s41699-023-00399-9]

Availability:

This version is available at: 11583/2980051 since: 2023-07-07T14:35:26Z

Publisher:

Springer Nature

Published

DOI:10.1038/s41699-023-00399-9

Terms of use:

This article is made available under terms and conditions as specified in the corresponding bibliographic description in the repository

Publisher copyright

(Article begins on next page)

ARTICLE OPEN



Scalable and highly selective graphene-based ion-exchange membranes with tunable permselectivity

Anna Aixalà-Perelló^{1,2}, Alessandro Pedico¹, Marco Laurenti^{1,2}, Enrica Fontananova^{1,3}, Sergio Bocchini^{1,2}, Ivan Vito Ferrari² and Andrea Lamberti^{1,2}✉

Graphene oxide (GO) membranes have been proved to be ion-selective thanks to their oxidized functional groups, which are naturally present on its surface. This ion selectivity, together with good mechanical strength, low cost, and simple synthesis, makes GO a great alternative material to conventional costly polymers for the production of ion-exchange membranes. This work focuses on how to produce GO membranes as ion-exchange membranes with a scalable approach and tunable permselectivity. Their physicochemical properties were subsequently investigated by means of selected characterization techniques. Results showed that GO membranes present good ion selectivity and size exclusion towards monovalent cations, reaching a permselectivity of up to 96%. Interestingly, UV-light irradiation of GO membranes can also be proposed as a green reduction method. GO reduction increases the permselectivity due to both a decrease in the dimension of the nanochannels and a reduction in the swelling degree of the membranes. The addition of binders was also investigated to improve the membranes' mechanical properties. Finally, the ionic resistance of the membranes was measured by impedance spectroscopy, achieving $4.6 \Omega \text{ cm}^2$, orders of magnitude lower than the state-of-the-art graphene oxide-based membranes.

npj 2D Materials and Applications (2023)7:46; <https://doi.org/10.1038/s41699-023-00399-9>

INTRODUCTION

In the last 50 years, the CO₂ emissions linked to fuel combustion have increased progressively¹. Currently, the overwhelming majority of the world's total energy supply comes from non-renewable sources: oil, coal, and natural gas². The situation is critical and requires a different approach to avoid arriving at a point of no return.

The EU takes the energy issue seriously and has set up a strategy that should drastically cut greenhouse gas emissions to 80–95% by 2050³. To do that, it is necessary to reach a secure, competitive, and decarbonized energy system which is strongly focused on new renewable energy sources.

Different sustainable and green energy sources such as wind, solar, geothermal, biomass, ocean thermal, wave, and tidal are gaining importance since they are zero-emitting and nonpolluting. Among these, the so-called “blue energy” technologies have been highlighted for their specific properties. They can be considered secure, scalable, reliable, and, more importantly, constant, in contrast with intermittent renewable sources such as wind and solar. A prime example is salinity gradient power (SPG) which has obtained renewed attention thanks to the recent development of 2D nanomaterials⁴. When two solutions with different salinity are mixed, the Gibbs free energy of mixing is released. The principle behind this phenomenon is the increase of entropy of the system, without any variation of enthalpy, which leads to a free energy decrease. Academic research mainly carried out in laboratories estimates that the power at stake worldwide is ~1.9 TW, i.e., almost 80% of the total global demand for energy⁵.

To harvest this energy, the three foremost technologies are pressure retarded osmosis (PRO), reverse electrodialysis (RED), and capacitive mixing (CapMix)^{6–9}.

Among them, the most promising one is the RED, in which the concentration gradient, or chemical gradient, induces an ionic flow from the concentrated stream (source) to the non-concentrated one (drain). An ion-exchange membrane (IEM) placed between two streams will interact with the ions of the salt, letting the counter-ions pass and repulsing the co-ions¹⁰. This process is based on the interaction of the membrane with the ions, producing an unbalanced movement of ions across the membrane, leading to a charge separation that will cause a potential difference. The potential difference achieved will generate redox reactions at the surface of two electrodes connected by an external circuit, generating a net current flow.

Compared to other energy sources, higher yields in terms of energy generation (around 60%^{11,12}) can be achieved considering the high selectivity of the membranes, as they allow direct conversion from chemical energy to electrical energy. The drawbacks of this technology are the reduction of membrane performance in the presence of highly concentrated and multivalent solutions; the trade-off between permselectivity and ionic resistance; and the membrane fouling¹⁰. The most important membrane properties concerning RED technology are high-ionic conductivity; high selectivity over counter-ions and co-ions; high-ion exchange capacity; high chemical and mechanical strength to maintain integrity in applications; antifouling properties; and acceptable cost^{10,13,14}.

The recent appearance of the 2D materials offers a great possibility to this technology as they overturn the operating mechanism of common polymeric membranes, and thus promise to overcome their current limitations¹⁵. The surface electrostatic charge of 2D materials plays a key role in their selectivity mechanism, due to the surface of these materials and the bulk effects being the same¹⁶. Materials like graphene, metal-dichalcogenides, and carbides have been investigated for membrane

¹Politecnico di Torino, Dipartimento di Scienza Applicata e Tecnologia (DISAT), Corso Duca Degli Abruzzi, 24, 10129 Torino, Italy. ²Istituto Italiano di Tecnologia, Center for Sustainable Future Technologies, Via Livorno 60, 10144 Torino, Italy. ³Institute on Membrane Technology of the National Research Council (ITM-CNR), at University of Calabria, Via P. Bucci, cubo 17/C, 87036 Rende (CS), Italy. ✉email: andrea.lamberti@polito.it

fabrication showing superior performance in ion selectivity, mechanical stability, and antifouling, despite, in the majority of the cases, being in experimental setups with a very small area^{17–19}.

Graphene oxide (GO) has become a focus in different fields of research due to its impressive properties, such as low mass density, excellent mechanical strength, ionic conductivity that can be tuned by means of specific functionalization, and high flexibility^{20–23}. GO membranes can easily be produced by vacuum filtration starting from a GO dispersion, resulting in easy-to-handle self-standing membranes²⁴. Moreover, even if the exploitation of GO in the RED field is at a small lab scale^{25–27}, the application of GO membranes to flexible electronics and water treatment has already achieved a high technology readiness level (TRL) with the fabrication of large-area membranes^{28,29}.

Ion sieving in GO membranes is achieved through both size and charge exclusion. Ion sieving by size is controlled by the interlayer distance between the GO flakes. The nanofluidic transport inside the channels is also governed by the surface properties of the 2D material³⁰. The intrinsic negative charge spontaneously present on GO membranes and the height of the lamellar nanochannels approaching the Debye screening length generate surface-charge-governed transport. Inside the channels, anions are repulsed while cations are attracted, leading to their permeation³¹. In addition, GO membranes show great selectivity towards different ions, resulting in asymmetric ion transport across the membranes due to the different diffusivities of the ions through the membranes^{32–34}.

GO membranes also have the ability to retain a concentration gradient between source and drain solutions for a long time, allowing the generation of the voltage difference needed to

produce the energy. Sun. et al. studied the anion transportation through GO membranes controlled by different cations. They found that cations are able to tune trans-membrane transportation of the anions and discovered that chlorides are the more suitable anions for energy generation applications³⁵.

Finally, GO can easily be functionalized in order to expose positive charges in order to obtain anion-exchange membranes. Recently, a small-scale all-graphene-based RED experiment has been reported by ref. ²⁵ with 0.8 mm² exposed area of the membrane, reaching power density values higher than 0.7 W m^{−2}.

Herein we report a scalable approach for the fabrication of a large-area GO membrane with high permselectivity toward cations for RED application, which achieved a higher ion transfer number and a much lower ionic resistance compared to the literature²⁵. The effect of the thickness and the lateral size of the GO flakes toward ion selectivity was carefully investigated, as well as the exploitation of suitable binders to allow higher stability of the membrane in water. The effect of the partial reduction of GO to reduced graphene oxide (rGO) exploiting UV-light illumination was carried out for the production of selective graphene oxide-based IEM.

RESULTS

Doctor blade as a scalable fabrication technique

One of the novelties of this study is the large-scale production of GO membranes (Fig. 1b). Doctor Blade technique allowed to produce scalable and homogeneous membranes (Fig. 1a). Gel homogeneity is required to obtain both the mechanical stability of

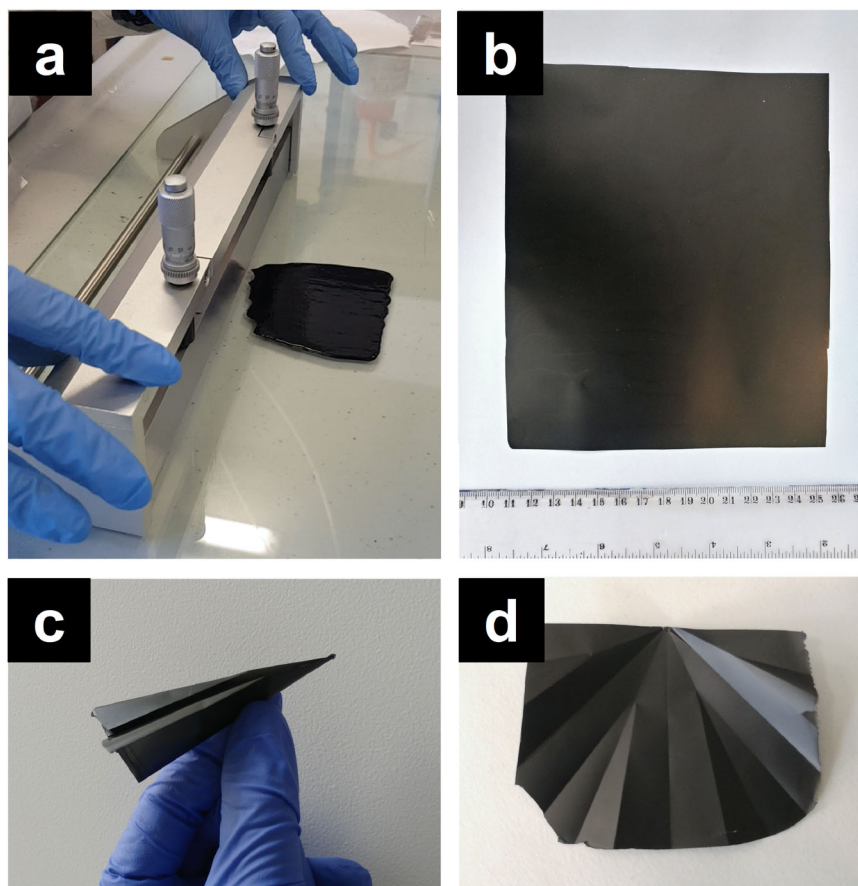
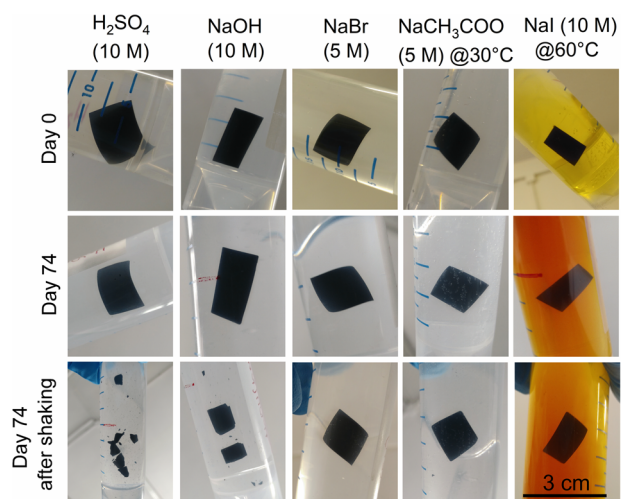


Fig. 1 Scalable GO membrane. **a** Production of GO membrane by Dr. Blade technique. **b** Scalable GO membrane of a dimension of 14.5 cm × 14.5 cm with a ruler in cm placed on the bottom. **c** Origami figure made of a GO membrane to show its mechanical resistance. **d** GO membrane after undoing the origami figure.

Table 1. Summary of the fabricated membranes considered within the work.

Name	Binder	UV-exposed time [min]	Thickness [μm]
GO-10	NA	NA	10 ± 1
GO-20	NA	NA	20 ± 3
GO-40	NA	NA	36 ± 2
GOPVDF-10	PVDF (10%)	NA	6 ± 0
GOPEO-10	PEO (10%)	NA	8 ± 1
Gochit-10	Chitosan (10%)	NA	8 ± 0
GOPVA-10	PVA (10%)	NA	8 ± 2
GOPVA-20	PVA (10%)	NA	14 ± 2
GOPVP-10	PVP (10%)	NA	8 ± 0
GOPVP-20	PVP (10%)	NA	21 ± 1
GOSPEEK10-10	SPEEK (10%)	NA	8 ± 1
GOSPEEK10-20	SPEEK (10%)	NA	16 ± 1
GOSPEEK20-20	SPEEK (20%)	NA	18 ± 2
rGO-UV10	NA	10	20 ± 1
rGO-UV20	NA	20	19 ± 1
rGO-UV30	NA	30	16 ± 2

**Fig. 2** Chemical stability of GO-20 membrane under different solutions. Membranes were tested during 74 days under static and dynamic conditions in H_2SO_4 10 M, NaOH 10 M, NaBr 5 M, NaCH_3COO 5 M, and NaI 10 M.

membranes, even when folded, and a defect-free upscaling production. Table 1 reports all studied membranes within this work.

GO membrane stability investigation and optimization

One of the most relevant issues of graphene membranes is their stability in solution. GO membranes were immersed in highly concentrated solutions (see experimental details and Fig. 2) whose nature and concentration were defined in order to test stressing conditions usually not tolerated by other IEMs^{36–38}. The GO membranes proved to be stable after two months, with the exception of the ones immersed in strongly acidic and basic solutions, getting partially destroyed after shaking the solutions (Fig. 2).

The thickness of the membrane plays an important role in membrane stability. 20- μm -thick membranes showed excellent stability in many harsh solutions (Fig. 2). However, when going towards lower thicknesses, the membranes showed poorer mechanical resistances.

The mechanical properties of GO membranes are strongly affected by hydration and dehydration processes. Water molecules easily diffuse into the matrix and swell the membranes³⁹. The addition of binders was proposed to strengthen the mechanical properties of the membranes, overcoming the lack of stability. PEO, PVA, and PVP were selected due to their solubility in water to produce solvent-free membranes. PVDF and chitosan were tested because they are commonly used for membrane production. SPEEK was proposed because of its well-known ion-selective properties. As shown in Fig. 3, composite membranes with PVA, PVP, and SPEEK were not destroyed after having been shaken in water for 1 min⁴⁰. Among all, PVA and PVP composites were the ones showing the highest mechanical resistance. They proved to be easy to handle in a wet state, and also in organic solvents such as propylene carbonate (Supporting Fig. 14).

FESEM analysis showed a uniform stacking of the flakes inside the membranes (Fig. 4a–c). Different membrane thicknesses can be obtained by increasing the blade gap of the Dr. Blade (Fig. 4a–c). An upper limitation was found at 50 μm , where the homogeneity of the Dr. Blade spread can no longer be guaranteed. The top surface of the membrane exhibits a planar morphology with wrinkles associated with GO flakes assembly (Fig. 4d). A rolled edge of the membrane (Fig. 4e) restates the good mechanical stability of the membranes.

PVP and SPEEK composite membranes showed great homogeneity (Fig. 5b, c). On the contrary, different agglomerates were found in the GOPVA-20 membrane matrix (Fig. 5a). An EDX mapping of the GOSPEEK10–20 (Fig. 5d–f) showed good dispersion of sulfur from SPEEK and sodium from the activation step of the polymer through all the membrane matrix, confirming the uniform distribution of the SPEEK inside the membrane structure.

Physical-chemical characterization of GO membrane

The zeta potential of the GO dispersion was investigated to assess its possible exploitation as a negatively charged membrane, resulting in a zeta potential of -23 mV. An UV treatment has been proposed in order to induce a controlled reduction at the surface of the GO membrane^{41–45}. A lower interlayer distance of rGO membranes strongly impacts the ion selectivity^{46,47}, contemporarily diminishing the wettability and worsening the mechanical properties²². The direct irradiation of the membrane results in a bifacial membrane since the UV radiation does not penetrate all the membrane thickness. In this way, the oxidized side of the membrane is preserving the mechanical robustness.

XPS was exploited as a surface-sensitive technique to study the effect of UV-light irradiation on the surface chemistry of the GO membranes. Independently on the considered sample, the wide-energy XPS scan analyses (Supplementary Fig. 1) highlighted that carbon (C) and oxygen (O) are the main elements, as expected (Supplementary Table 1). Small traces of sulfur (S) coming from the GO dispersion manufacturing process were also detected. From XPS measurements, it is possible to see that after UV irradiation, there is a reduction of the O content in favor of the C content. Instead, membranes dried at 60 °C didn't show significant differences with GO dried at room temperature, meaning that the process can be fastened without changing the chemistry of the material (Supplementary Table 1).

The analysis of HR XPS spectra related to C 1s element confirmed the presence of a graphitic-like structure and the effective reduction of GO after the UV exposure (Fig. 6). According to the literature, the deconvolution of each spectrum into

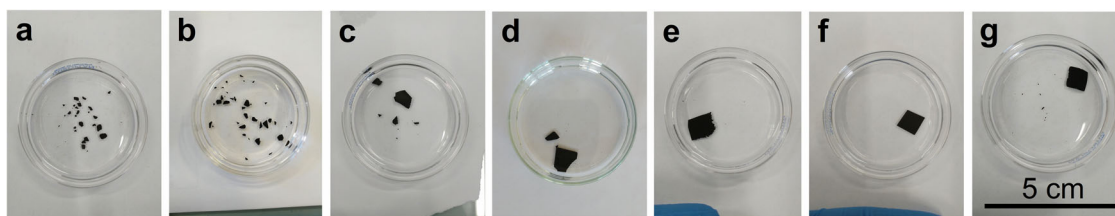


Fig. 3 Mechanical stability of thin composite membranes of a dimension of 1 cm² in water. a GO-10, **b** GOPVDF-10, **c** GOPEO-10, **d** GOchit-10, **e** GOPVA-10, **f** GOPVP-10, and **g** GOSPEEK10-10.

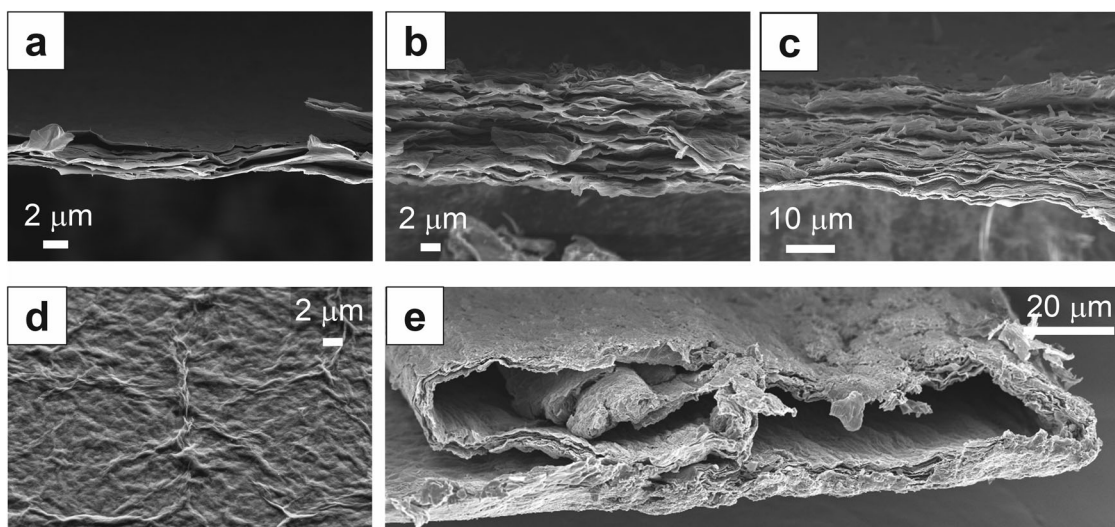


Fig. 4 FESEM analysis of GO membranes. a–c Cross-section of GO membranes with different thicknesses. **d** Top view of a GO membrane and **e** rolled edge of GO membrane.

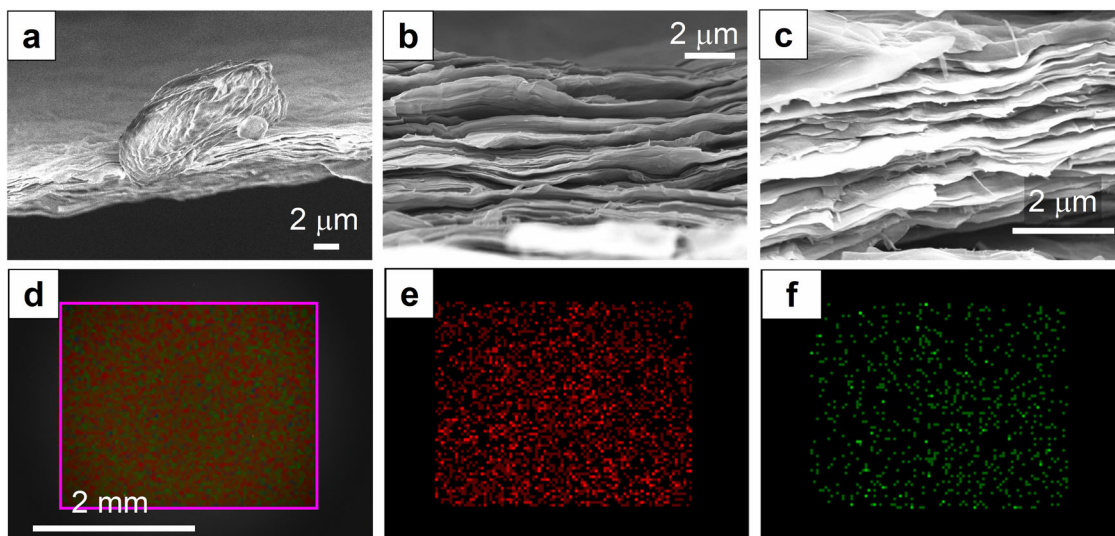


Fig. 5 Cross-section of composite membranes. a GOPVA-20 with a PVA agglomerate on its structure. **b** GOPVP-20 membrane. **c** GOSPEEK20-20. EDX mapping of S and Na in the GOSPEEK20-20 membrane matrix. **d** S and Na, **e** S, and **f** Na.

separate components was carried out^{48,49}. The two main peaks are those related to (i) carbon atoms arranged in a graphitic structure through C-C sp_2 sigma bonds, positioned at 284.5 eV; (ii) C atoms involved into C-O-C epoxy groups and/or bonded to hydroxyl groups (C-OH), positioned at 286.5 ± 0.1 eV. Additional components positioned at around 288.0 and 288.50 eV are found due to C atoms related to carbonyl C=O and carboxylic COOH functional groups, respectively. The effectiveness of UV light as a reducing

agent is confirmed by the decrease in the amount of C-O-C/C-OH functional groups for UV-treated GO membranes compared to the non-treated GO one (Supporting Table 2). The appearance of a satellite peak (shake-up) at 291.0 ± 0.5 eV is due to a π - π^* transition typical of graphitic-like materials and is observed only for the UV-treated membranes.

These findings were confirmed by FTIR spectroscopy analysis, which showed changes in the functional groups of GO (Fig. 6e).

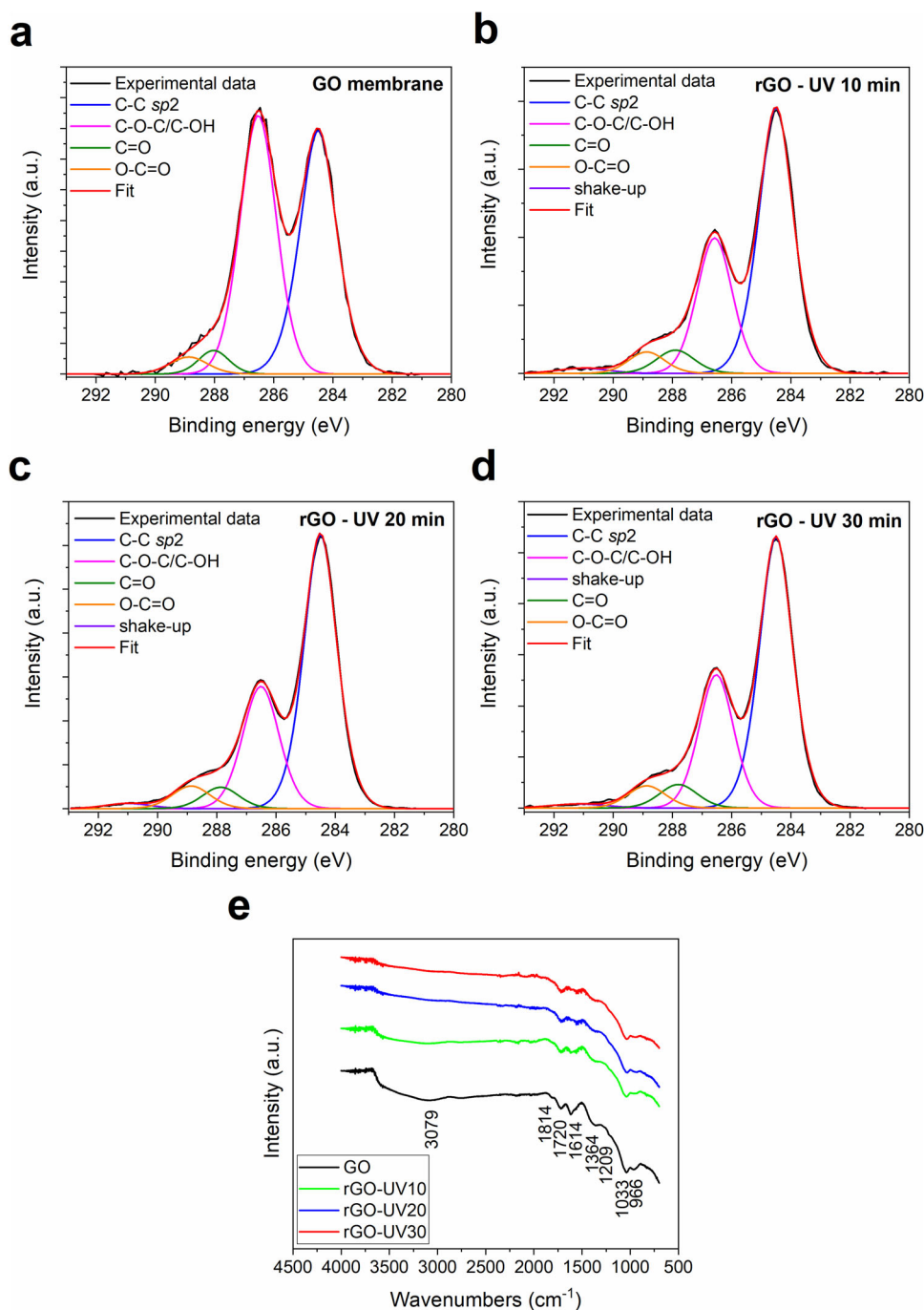


Fig. 6 High-resolution C 1s XPS spectra of GO membranes. **a** As-prepared, **b–d** after UV-light irradiation for 10, 20, and 30 min. **e** Evolution of the IR spectrum of GO after UV-light irradiation at different times.

According to literary data^{50–52}, the absorption band at $3000\text{--}3700\text{ cm}^{-1}$ is related to the stretch vibrations of the O-H bonds. The peak at 1720 cm^{-1} corresponds to the stretch vibrations of the carboxyl group ($\text{C}=\text{O}$). The peak of the aromatic ring ($\text{C}=\text{C}$) is associated with the one at 1614 cm^{-1} . Hydroxyl (O-H) groups are related to the peak at 1364 cm^{-1} . The vibrations of the C-OH bonds are associated with the 1209 cm^{-1} peak. The absorption band at 1033 cm^{-1} relates to the stretch vibrations of alkoxy groups ($\text{C}-\text{O}$)³¹. Finally, the peak at 966 cm^{-1} has been reported to be related to the deformation vibrations of the epoxy groups. From this analysis, it can be noticed that the reduction of

the GO by UV light significantly affects the hydroxy and epoxy groups, as highlighted also by XPS spectra.

XRD measurements confirmed that by increasing the reducing time, the interlayer distance is lowered (see Table 2 and Fig. 7). A saturation point is reached at 20 min of reduction time as no significant differences were detected between the results at 20 and 30 min. All the membranes showed a larger interlayer distance in a wet state because of the swelling and the water intake phenomena (Fig. 7b). Nevertheless, rGO membranes were able to keep smaller interlayer distances because of their hydrophobic nature and their initial smaller interlayer distance.

Table 2. Interlayer distances [\AA] of GO and rGO membranes in a dry and wet state.

	Dry	Wet
GO-20	8.3	14.0
rGO-UV10	8.0	12.0
rGO-UV20	7.8	11.5
rGO-UV30	7.9	11.5
GOPVA-20	9.4	13.5
GOPVP-20	9.0	15.8
GOSPEEK10-20	9.3	NA
GOSPEEK20-20	9.1	NA
GO + NaCl	8.3	12.9

Composite membranes showed larger interlayer distances in the dry state (Fig. 7c). When wet, GOPVA-20 presented a slightly smaller interlayer distance, while in the case of GOPVP-20, it was bigger (Fig. 7d). Due to the swelling of SPEEK, XRD measurements in wet state of these composite membranes could not be pursued. In order to have a more accurate measurement of the interlayer distance of GO membranes in a real application, a GO membrane with NaCl ion present inside the structure was measured in both dry and wet states (Fig. 7e, f). While in the dry state, no differences were noticed, in the wet state, the membrane showed a smaller interlayer distance in the presence of a salty solution (NaCl 0.5 M). Liang Chen et al.³² demonstrated a cationic control of the interlayer spacing thanks to the interaction between the hydrated cation and the graphene oxide sheets. Likewise, Young Hoon Cho et al. demonstrated that the interlayer distance in GO membranes varies with ion concentration and hydrated ion size³⁹.

From Table 3, it is possible to appreciate the increase of the water contact angle by increasing the irradiation time. Since the light is reducing the GO, the wettability is reduced due to an increase in hydrophobicity. Surface energy values show a reduction of the surface energy mainly ascribable to the polar components.

Electrochemical characterization of GO membranes: permselectivity and ionic resistance

GO membranes showed a selective permeability towards cations due to the negative charge of the GO. Permselectivity was measured with and without the ion transport number correction (α_{ap} and α_{tn} , respectively, Eqs. 1 and 2 in the Methods section) and with and without the contribution of the junction potential. Given that KCl was selected as the main salt, no significant changes were obtained considering the ion transport number correction in the permselectivity calculations, as the diffusion coefficients of K^+ and Cl^- are similar (1.957×10^{-5} and $2.032 \times 10^{-5} \text{ cm}^2 \text{ s}^{-1}$, respectively⁵³). Instead, the junction potential remarkably changed the final permselectivity results. All measurements have been normalized to the results obtained for GO-20 (Table 4).

As shown in Supporting Fig. 13, preliminary results show that these membranes are selective towards monovalent ions, being Na^+ and K^+ the ones achieving better performances as they have a smaller hydrated radius. P. Sun et al.³⁵ and Young Hoon Cho et al.³⁹ demonstrated that monovalent ions have stronger interactions with GO membranes. The ion permeability of such ions depends on the ion sorption capability, not on the diffusivity of the ions. In the presence of divalent ions, a reduction of the Donnan potential is reported. Contemporarily, a lower interaction inside the membrane is observed due to the screening effect of the water molecules around the cations, resulting in faster migrations of anions through the GO membrane, leading to a lower permselectivity. Anyway, a specific study of the performance

of these membranes as monovalent-selective is out of the scope of this study.

GO membranes exhibited different permselectivity performances depending on the concentration gradients (Fig. 8). It is well known in the literature that when increasing the ionic strength of the external solutions, the permselectivity tends to decrease because of the higher difference in ion activity between the electrolyte solution and the membrane phase, resulting in a concentration driven (i.e., diffusive) transport of the co-ion³⁶, reducing the permselectivity. When the negatively charged surface of the GO membrane is exposed to the electrolyte, cations accumulate on the surface of the channels, creating a double layer. When increasing the concentration, the screening effect will become more significant up to the point that the center of the channel is electrically neutral, therefore losing selectivity.

On the contrary, results show a decrease in permselectivity at higher folds, when the diluted stream becomes more diluted. Liang Chen et al.³² demonstrated that strong cation- π interactions between hydrated cations Na^+ and K^+ and the aromatic ring of GO reduces the interlayer spacing of GO membranes. GO membranes' channels change not only in dimension but also in channels' surface-charge when the solution fills the channels. Therefore, when working in diluted concentrations, (i.e., 0.01 M in the 100-fold measurement) the membranes showed proneness to exfoliate, becoming more fragile. In fact, swelling is controlled by ion intercalation at concentrations higher than 0.1 M ³⁹. Therefore, when working with diluted solutions, membrane swelling also plays an important role by reducing the permselectivity.

A strong improvement of the permselectivity was achieved by moving from a membrane thickness of $10 \mu\text{m}$ to a membrane of $30 \mu\text{m}$ (Fig. 9a). Thicker membranes showed better ion exclusion because of a lower ion permeation⁵⁴, higher stability in water, and reduced swelling degree. Higher thicknesses were not tested given that ionic resistance, explained below, increases significantly.

Previous studies have demonstrated a strong effect of the lateral size of the GO flakes on the nature of the functional group exposed^{54–56}. Together with the 2D channel dimension, they will be the main actors in the ion exclusion. For this reason, the effect of the lateral size was investigated. Different size ranges were determined from the centrifugation separation, being $>20 \mu\text{m}$, $2–20 \mu\text{m}$, and $<2 \mu\text{m}$ the ones corresponding to the centrifugation velocities of 1000, 2000, and 3000 rpm, respectively (Fig. 9c–e).

The lateral size of the flakes was demonstrated to affect the performance of the membranes (Fig. 9b). The ion penetration is enhanced when lowering the size of the flakes due to an increase of the nano-capillaries⁵⁴. Instead, when enlarging the flakes, the pathways of the ions will become more tortuous, thus slowing the ion transport¹⁶.

Composite membranes with binders were studied in terms of permselectivity. The membranes showing higher performances are the ones with binders, thanks to their improved mechanical stability in water, as shown in Fig. 3 and Supplementary Fig. 14.

The reduction of GO membranes showed an improvement in performance. As stated in Table 2, the interlayer distance at the surface of the membranes is reduced due to the partial removal of the oxygen-containing groups. This reduction not only affects the interlayer distance, but also the hydrophilicity of the membranes by reducing the water absorption capacity of the membrane⁵⁷. Given that the hydrated ions (co-ions and counter-ions) diffuse through the channels partially thanks to the hydrophilic nature of the membrane, selectivity is enhanced by both the pore shrinking and the more hydrophobic nature of the membrane. Permselectivity measurements show a saturation point of the permselectivity at 10 min reduction time (Fig. 10c).

The cation transference number was evaluated to compare the performance of the presented membranes to previous works (see Supplementary Eq. 1). It is worth mentioning that, in a

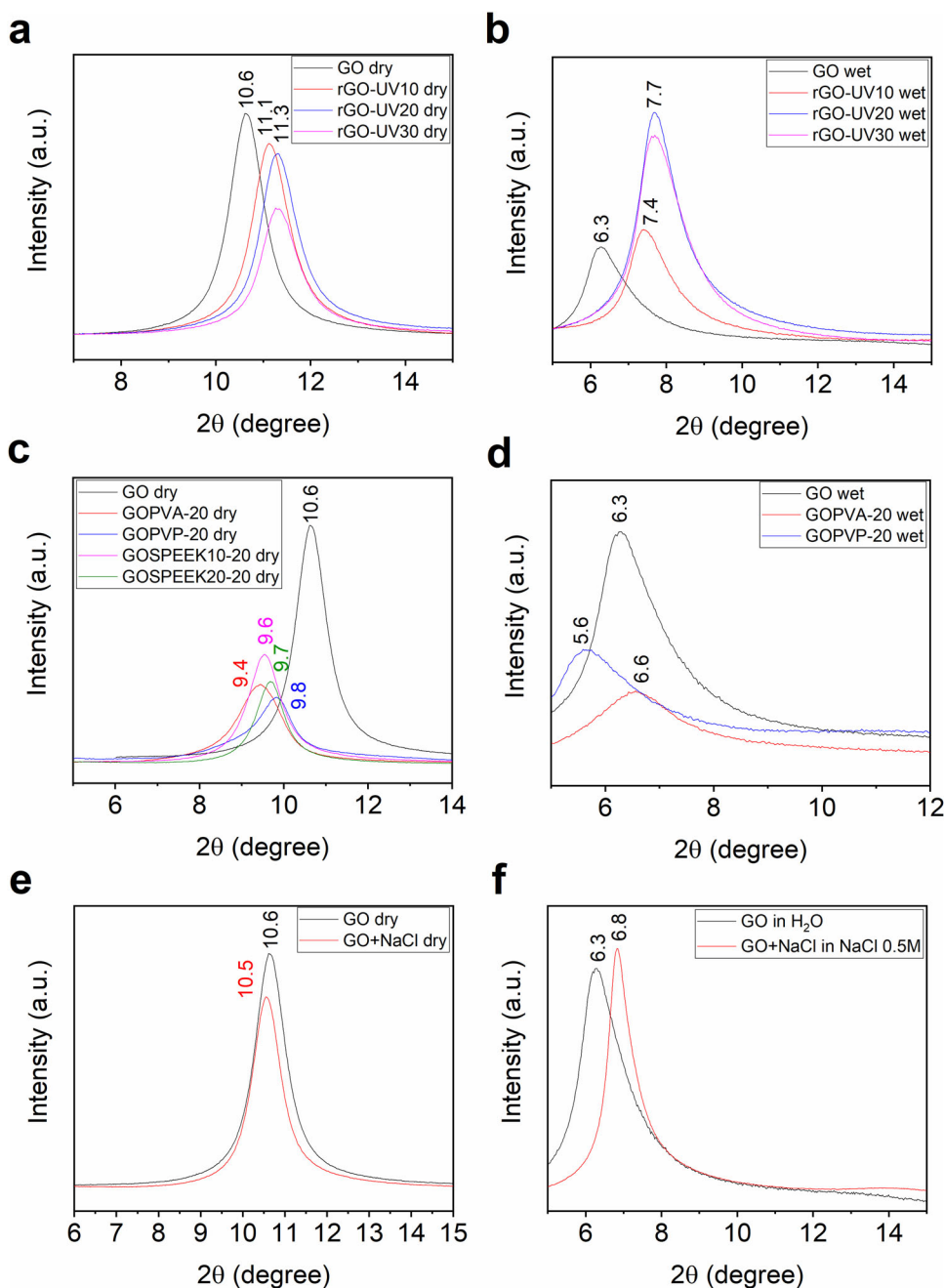


Fig. 7 XRD measurement of GO membranes reduced at 0, 10, 20, and 30 min. **a** Dry, **b** wet states, composite membranes in **c** dry **d** wet states, and GO membrane and GO with NaCl salt inside the channels in **e** dry **f** wet states.

concentration gradient of 5 folds, a cation transference number of 0.97 was obtained for GO-20, which is significantly higher than the 0.6 value reported in the state-of-the-art of GO membranes²⁵.

The ionic resistance of the GO membranes was evaluated, being one of the most important parameters for their successful implementation as IEMs. The values obtained were three orders of magnitude lower compared to the ones previously reported^{25,26}. EIS measurements show that the ionic resistance is strongly dependent on the thickness of the membranes. When doubling the thickness (from GO-20 to GO-40), ionic resistance increased from 4.6 to 12 $\Omega \text{ cm}^2$. PVP and SPEEK did not significantly affect the ionic resistance of the membrane. Instead, PVA increased membrane resistance. This has been attributed to the non-homogeneous PVA distribution (Fig. 5a) through the GO matrix and a smaller interlayer distance of the pores of GOPVA-20

in the wet state compared to GO-20 or GOPVP-20. Likewise, rGO-UV20 presented a higher ionic resistance due to its smaller channels.

The variation of the trend of the spectra at high frequencies with time (Supplementary Figs. 5–11) suggests that the filling of the pores with water is reaching stability after 30 min of immersion (Fig. 11a). These results show a dominant effect of the solution inside the membrane pores. It is worth mentioning that the membranes kept reducing their resistance over time, up to 3.9 $\Omega \text{ cm}^2$ after 90 min in the case of GO-20. On the contrary, polymeric membranes show an increase in resistance over time. Higher resistance variations were detected in the reduced and composite membranes at time 0, suggesting a lag of electrolyte permeation. A maximum power density of 0.54 W m^{-2} has been

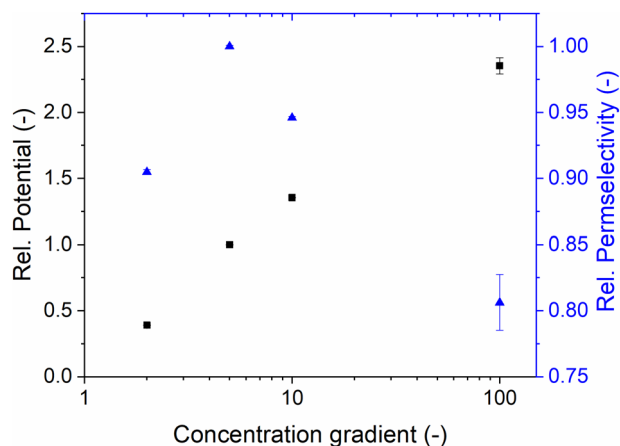


Fig. 8 Normalized potential and permselectivity of GO-20 membrane under different concentration gradients. A fixed concentrated solution of KCl 1 M was selected. Error bars correspond to the standard deviation of each measurement.

Table 3. Contact angle and surface energy parameters of the membranes were evaluated with the OWRK model together with the separate contributions of dispersive and polar components.

	Contact angle (°)		Surface energy (mJ m ⁻²)		
	H ₂ O	CH ₂ I ₂	SE	Disp	Polar
GO-20	60.6	33.9	47.34	34.86	12.48
rGO-UV10	67.7	34.6	43.76	35.26	8.51
rGO-UV20	71.1	35.2	42.57	35.91	7.43
rGO-UV30	76.4	36.7	41.51	35.83	5.68

Table 4. Potential and permselectivity measured values.

	Potential (mV)	$\alpha_{ap,NO\ Ej}$ (%)	$\alpha_{ap,Ej}$ (%)	$\alpha_{tn,NO\ Ej}$ (%)	$\alpha_{tn,Ej}$ (%)
GO-20	-34.55	93.3	91.2	93.5	91.3
Permselectivity is shown with and without incorporating the ion transport number correction and the junction potential.					

achieved for GOPVP-20, the best-performing membrane in terms of electrochemical properties and mechanical stability.

DISCUSSION

Scalable graphene oxide-based membranes have been fabricated by the doctor blade approach as cation exchange membranes for reverse electrodialysis applications. Different cumulative parameters have been investigated: the thickness; the UV-light exposure as a chemical-free reduction mechanism; the lateral size; and the permselectivity, reaching a maximum of 96%.

The use of binders was proposed to strengthen the mechanical stability of the membranes, being the composites with PVA and PVP the most mechanically resistant in strongly acidic and alkaline solutions, also after several months.

In terms of ionic resistance, GO-20 presented an ionic resistance of 4.6 Ω cm², which increased with thickness and reduction time. Ionic resistance was identified to be strongly affected by the electrolyte solution inside the GO channels. This resistance can be reduced to a minimum of 3.9 Ω cm², increasing the incubation

time. This value is comparable to commercial membrane values and almost four times lower than previously reported GO membranes. PVP and SPEEK did not show considerable differences compared to self-standing GO, while PVA worsened the performance due to a pore shrinking and a non-homogeneous distribution of the polymer inside the membrane. Finally, it is noteworthy to underline an outstanding cation transference number of 0.97 with a concentration gradient as low as fivefold, achieving a maximum power density of 0.54 W m⁻².

METHODS

Materials

GO dispersion (2.5 wt%) was purchased from Graphenea. All the chemicals and polymers were supplied by Merck. The chemical reagents employed for this study were lithium chloride (LiCl, ≥99%), dimethyl sulfoxide (DMSO, >99.5%), sodium chloride (NaCl, ≥99%), potassium chloride (KCl, ≥99%), calcium chloride (CaCl₂, ≥99%), magnesium chloride (MgCl₂, ≥98%), sodium bromide (NaBr, ≥99%), sulfuric acid (H₂SO₄, 95–98%), sodium hydroxide (NaOH, ≥98%), sodium acetate (NaCH₃COO, ≥99%), and sodium iodide (NaI, ≥99%). The polymers employed in this study were chitosan (M_w 310000–375000), poly(vinyl alcohol) (PVA, M_w 310000–375000), polyvinylpyrrolidone (PVP, M_w 10000), polyether ether ketone (PEEK, M_w 20800), and poly(ethylene oxide) (PEO, M_w 100000).

Synthesis of sulfonated polyether ether ketone (SPEEK)

The SPEEK was prepared by dissolving 8 g of PEEK in 50 mL of sulfuric acid 95–97%. The polymer slowly dissolved, forming a red viscous solution. After 96 h, the solution was slowly added dropwise in a large excess of cold deionized water. After standing overnight, the precipitate was filtered and washed several times with deionized water and thus dried at 60 °C in a vacuum oven until constant weight. The SPEEK was subsequently immersed in NaCl 0.5 M overnight in order to exchange the proton of the sulfonic group with the Na⁺.

Membrane fabrication

Doctor Blade technique was studied as an alternative scalable method compared to the ones commonly used for the fabrication of GO membranes (i.e., vacuum filtration). The GO gel supplied by Graphenea was cast on a glass support, varying the thicknesses from 0.5–3 mm, and dried at room temperature. Thermal treatment at 60 °C was also investigated to fasten the drying process of the membrane. This step allowed to reduce the drying time of the membrane from 5 h to only 30 min without affecting the chemistry of the membrane (see Supporting Information for further details).

The addition of binders into the GO structure was studied to increase its mechanical strength. PVA, PEO, PVP, PVDF, chitosan, and SPEEK were tested using a 10:1 weight ratio of GO:binder. Shortly, the binder was first solvated and then added in the proper ratio to the GO gel. The final GO concentration was 16.67 mg mL⁻¹. The obtained gel was stirred overnight and a high vacuum was applied afterward to remove bubbles to ensure homogeneity, a mandatory requirement to avoid defects in the membrane. Water was used as a solvent for PVA, PEO, PVP, and PVDF. SPEEK was solubilized in DMSO using a concentration of 50 mg mL⁻¹ and water was used to reach the final GO concentration. Chitosan's concentration was 20 mg mL⁻¹ in a 1 wt% solution of acetic acid⁵⁸.

rGO by UV light

UV light (UV solar simulator, Newport) was investigated as a reducing method to control the functional groups at the surface of the membranes. UV light with an intensity of 6.37 W cm⁻² was used with different exposure times on the surface of the membranes, achieving different reduction degrees.

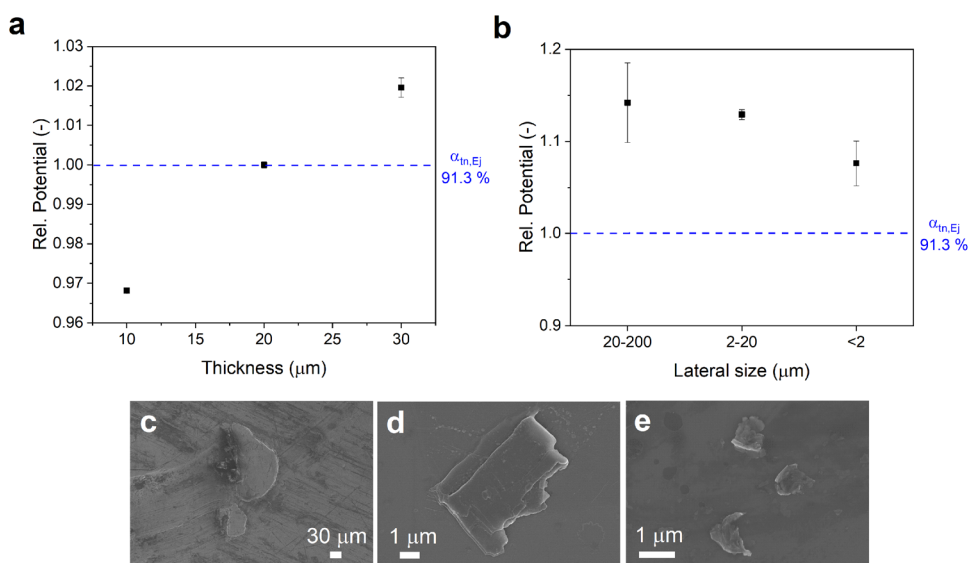


Fig. 9 Permselectivity of GO membrane in NaCl 0.1/0.5 M as a function of. **a** thickness **b** lateral size. Error bars correspond to the standard deviation of each measurement. Graphene oxide flakes were obtained after centrifugation at **c** 1000 rpm, **d** 2000 rpm, and **e** 3000 rpm.

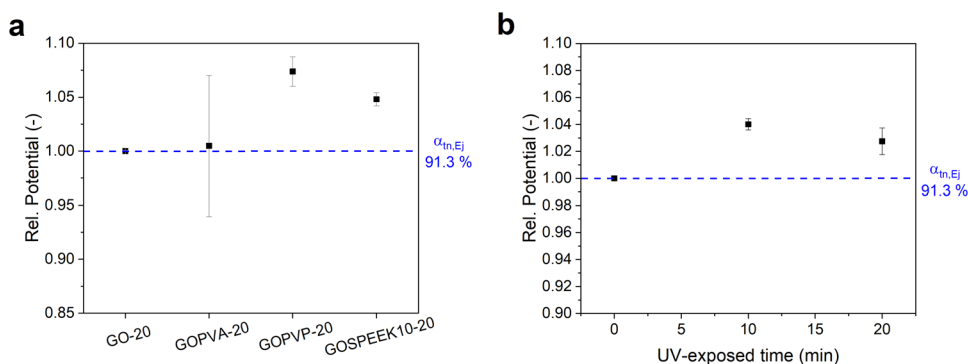


Fig. 10 Permselectivity of membranes in KCl 0.1/0.5 M. **a** with different binders **b** GO-20 under different reduction times. Error bars correspond to the standard deviation of each measurement.

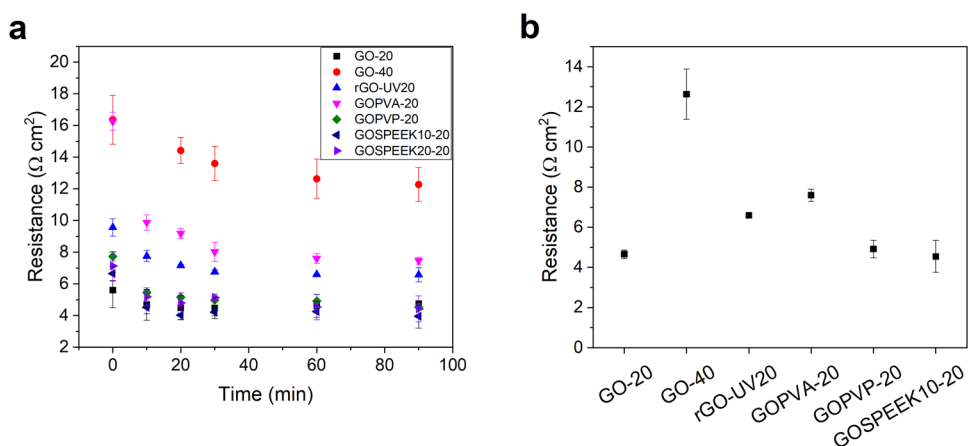


Fig. 11 Membrane areal-resistance. **a** as a function of time **b** after 1 h in solution. Error bars correspond to the standard deviation of each measurement.

Characterization methods

Z-potential was measured by Litesizer 500 (Anton Paar) on solutions of GO with a concentration of 0.05 mg mL⁻¹ in order to confirm the presence of negative charges on the surface of GO

flakes. To investigate the chemical stability of membranes, they were immersed under different acidic and alkaline solutions (H₂SO₄ 10 M, NaOH 10 M, NaBr 5 M, NaCH₃COO 5 M, and NaI 10 M). GO pieces of 1 cm² were soaked under each solution for

70 days. After the immersion, they were shaken for 1 min and examined.

The morphology of both membranes and flakes was investigated by Field-Emission Scanning electron microscopy (FESEM Supra 40, manufactured by Zeiss). The cross-section was also inspected to check the homogeneity along the thickness. At the same time, the thickness of the membranes was measured to verify the repeatability of the preparation process. The effect of the lateral size was investigated to understand its possible impact on permselectivity. To do so, an aqueous GO dispersion was centrifugated at different velocities (1000, 2000, and 3000 rpm) in order to separate flakes with different lateral sizes.

The reduction of the GO by UV-light was analyzed by Fourier transform infrared (FTIR) spectroscopy (Nicolet 5700 FTIR, Thermo Fisher Scientific), contact angle measurement (OCA H200 DataPhysics equipment), and X-Ray diffraction (XRD, X'Pert pro, Malvern Panalytical). For the FTIR analysis, all the membranes were kept under vacuum for 24 h to avoid the contribution from atmospheric moisture.

The surface chemistry of the membranes was investigated by X-Ray Photoelectron Spectroscopy (XPS), with a PHI 5000 VersaProbe (manufactured by Physical Electronics) equipped with Al K α radiation (1486.6 eV) as an X-ray source. Wide-energy and high-resolution (HR) XPS spectra were processed using CasaXPS software (version 2.3.18). HR C1s core level spectra deconvolution into mixed Gaussian-Lorentzian individual components was obtained after binding energy (BE) calibration according to C1s position for graphitic C-C bonds (284.5 eV) and Shirley background subtraction.

Interlayer distances between flakes of GO membranes were determined by XRD. The measurement has been performed in Bragg-Brentano 2 θ configuration, using a Cu source. With this setup, the peak related to the interlayer distance of GO membranes is typically observed for angles of 5°–14°. From the peak value, the interlayer is directly evaluated using the Bragg law. Typical values are below 1 nm for dry membranes, while slightly above 1 nm for wet ones. Membranes were tested in both dry and wet states. The wet samples were immersed in deionized water for 1 h at room temperature before the measurement.

The hydrophobicity of the membranes was checked by contact angle measurement of the GO and rGO membranes. Water and diiodomethane were selected as test liquids to evaluate the surface energies of the membranes (Supporting Fig. 3).

The apparent permselectivity of the membrane is one of the most important parameters for an IEM. This figure of merit was used to define the best-performing material among the ones under study. In literature, the apparent permselectivity of the membrane can be calculated with or without the ion transport numbers of the ions in the solution^{36,59}. In this study, both will be calculated to be comparable to what has been previously done.

$$\alpha_{\text{ap}} = \frac{E_{\text{mem}}}{E_{\text{the}}} \quad (1)$$

$$\alpha_{\text{tn}} = \frac{\frac{E_{\text{mem}}}{E_{\text{the}}} + 1 - 2t_g}{2t_c} \quad (2)$$

where E_{mem} is the potential across the membrane, E_{the} ^{38,60–64} is the potential of an ideally selective membrane calculated from the Nernst equation (Supporting Eq. 2 and Supporting Table 3) and t_g and t_c are the transport numbers of the counterions and co-ions, respectively. The ion transport numbers were calculated from ion diffusion coefficients as previously reported in refs.^{38,53}.

The potential difference between the two Ag/AgCl reference electrodes (E_{offset}) and the potential difference between the reference electrodes and the electrolyte solution (known as junction potential, E_j) were subtracted from the measured potential at the membrane (E_{meas}). Junction potential was

calculated from the Henderson equation³⁸ (Supporting Eq. 3 and Supporting Table 4). The potential across the membrane is therefore determined from Eq. 3:

$$E_{\text{mem}} = E_{\text{meas}} - \Delta E_{\text{offset}} - \Delta E_j \quad (3)$$

The measurement setup consisted of a side-by-side cell with a membrane separating two chambers containing electrolytes at different concentrations. Typically, KCl flowed at a flow rate of 5 mL/min at 0.1 M and 0.5 M concentrations. Nevertheless, LiCl, NaCl, CaCl₂, and MgCl₂ were tested to see the performance of the membranes toward different cations. Each chamber has a volume of 25 mL with a hole diameter of 1.5 cm where the membrane is placed. Ag/AgCl reference electrodes were used to measure the potential across the membrane (Supporting Fig. 12a, b).

The ionic resistance of the membranes was measured by electrochemical impedance spectroscopy (EIS)⁶⁵ in a four-electrode configuration using a potentiostat/galvanostat combined with a frequency response analyzer (Metrohm M101 Autolab). EIS was selected to avoid the non-ohmic contribution of the resistance due to the concentration changes given by the transport of the ions under the influence of the electrical current and the membrane polarization. A home-designed two-chamber setup was used (Supporting Fig. 12c), each chamber with a volume of 30 mL and a membrane area of 1.8 cm². Both sides were filled with NaCl 0.5 M in static mode. The potential drop across the membrane was measured by Ag/AgCl reference electrodes positioned in Haber-Luggin capillaries, filled with NaCl 0.5 M. Titanium foils were used as working and counter electrodes. A frequency sweep from 10³ to 0.1 Hz was performed, with a signal amplitude of 5 mV. At high frequencies, the intercept of the curve on the real axis corresponds to the resistance of the membrane and the solution. The membrane resistance is obtained by subtracting the blank (i.e., the resistance obtained with the cell filled only with the testing solution and without the membrane). The blank corresponds to the ohmic contribution part of the electrical resistance due to the feed waters. Both electrochemical setups were validated with the FKS-30 membrane from Fumatech. The permselectivity and the ionic resistance obtained were in accordance with the specifications of the manufacturer.

Maximum potential density (PD_{max})⁶⁶ was calculated from Eq. 4. This value is related just to the performance of the ionic membranes without considering the contribution of the cell.

$$\text{PD}_{\text{max}} = \frac{E_{\text{mem}}^2}{4R_m} \quad (4)$$

E_{mem} is the open-circuit potential measured during the permselectivity measurement and R_m is the ionic resistance obtained for each membrane, without the contribution of the feed waters nor the non-ohmic part of the membrane resistance.

DATA AVAILABILITY

The data that support the findings of this study are available from the corresponding author upon reasonable request.

Received: 11 January 2022; Accepted: 18 May 2023;

Published online: 03 July 2023

REFERENCES

- Harris, S., Weinzettel, J., Bigano, A. & Källmén, A. Low carbon cities in 2050? GHG emissions of European cities using production-based and consumption-based emission accounting methods. *J. Clean. Produ.* **248**, 119206 (2020).
- Papadis, E. & Tsatsaronis, G. Challenges in the decarbonization of the energy sector. *Energy* **205**, 118025 (2020).
- Oettinger, G. H. *Roadmap 2050* (European Commission, 2012).

4. Siria, A., Bocquet, M. L. & Bocquet, L. New avenues for the large-scale harvesting of blue energy. *Nat. Rev. Chem.* **1**, 0091 (2017).
5. Ramon, G. Z., Feinberg, B. J. & Hoek, E. M. V. Membrane-based production of salinity-gradient power. *Energy Environ. Sci.* **4**, 4423 (2011).
6. Achilli, A., Cath, T. Y. & Childress, A. E. Power generation with pressure retarded osmosis: an experimental and theoretical investigation. *J. Membr. Sci.* **343**, 42–52 (2009).
7. Mei, Y. & Tang, C. Y. Recent developments and future perspectives of reverse electrodialysis technology: a review. *Desalination* **425**, 156–174 (2018).
8. Brogioli, D. Extracting renewable energy from a salinity difference using a capacitor. *Phys. Rev. Lett.* **103**, 058501 (2009).
9. Tufa, R. A. et al. Progress and prospects in reverse electrodialysis for salinity gradient energy conversion and storage. *Appl. Energy* **225**, 290–331 (2018).
10. Hong, J. G. et al. In *Advanced Nanomaterials for Membrane Synthesis and its Applications* (eds Lau, W., Ismail, A., Isloor, A. & Al-Ahmed, A.) Ch. 13 (Elsevier Inc., 2018).
11. Yip, N. Y., Vermaas, D. A., Nijmeijer, K. & Elimelech, M. Thermodynamic, energy efficiency, and power density analysis of reverse electrodialysis power generation with natural salinity gradients. *Environ. Sci. Technol.* **48**, 4925–4936 (2014).
12. Vermaas, D. A. et al. High efficiency in energy generation from salinity gradients with reverse electrodialysis. *ACS Sustain. Chem. Eng.* **1**, 1295–1302 (2013).
13. Güler, E., Elizen, R., Vermaas, D. A., Saakes, M. & Nijmeijer, K. Performance-determining membrane properties in reverse electrodialysis. *J. Membr. Sci.* **446**, 266–276 (2013).
14. Hong, J. G. et al. Potential ion exchange membranes and system performance in reverse electrodialysis for power generation: a review. *J. Membr. Sci.* **486**, 71–88 (2015).
15. Das, R. (ed.) *Two-Dimensional (2D) Nanomaterials in Separation Science* (Springer, 2021).
16. Caglar, M. & Keyser, U. F. Ionic and molecular transport in aqueous solution through 2D and layered nanoporous membranes. *J. Phys. D Appl. Phys.* **54**, 183002 (2021).
17. Gugliuzza, A., Politano, A. & Drioli, E. The advent of graphene and other two-dimensional materials in membrane science and technology. *Curr. Opin. Chem. Eng.* **16**, 78–85 (2017).
18. Moghadam, F. & Park, H. B. 2D nanoporous materials: membrane platform for gas and liquid separations. *2D Mater.* **6**, 042002 (2019).
19. Macha, M., Marion, S., Nandigana, V. V. R. & Radenovic, A. 2D materials as an emerging platform for nanopore-based power generation. *Nat. Rev. Mater.* **4**, 588–605 (2019).
20. Zhu, Y. et al. Graphene and graphene oxide: synthesis, properties, and applications. *Adv. Mater.* **22**, 3906–3924 (2010).
21. Joshi, R. K., Alwarappan, S., Yoshimura, M., Sahajwalla, V. & Nishina, Y. Graphene oxide: the new membrane material.pdf. *Appl. Mater. Today* **1**, 1–12 (2015).
22. Ma, J., Ping, D. & Dong, X. Recent developments of graphene oxide-based membranes: a review. *Membranes* **7**, 52 (2017).
23. Baudino, L. et al. Crown-ether functionalized graphene oxide membrane for lithium recovery from water. *Membranes* **12**, 233 (2022).
24. Pedico, A. et al. Graphene oxide membranes for trace hydrocarbon contaminant removal from aqueous solution. *Nanomaterials* **10**, 2242 (2020).
25. Ji, J. et al. Osmotic power generation with positively and negatively charged 2D nanofluidic membrane pairs. *Adv. Funct. Mater.* **27**, 1603623 (2017).
26. Jia, P. et al. The combination of 2D layered graphene oxide and 3D porous cellulose heterogeneous membranes for nanofluidic osmotic power generation. *Molecules* **26**, 5343 (2021).
27. Zhang, Z. et al. Vertically transported graphene oxide for high-performance osmotic energy conversion. *Adv. Sci.* **7**, 2000286 (2020).
28. Akbari, A. et al. Large-area graphene-based nanofiltration membranes by shear alignment of discotic nematic liquid crystals of graphene oxide. *Nat. Commun.* **7**, 10891 (2016).
29. Zhong, J. et al. Efficient and scalable synthesis of highly aligned and compact two-dimensional nanosheet films with record performances. *Nat. Commun.* **9**, 3484 (2018).
30. Quintano, V. et al. Long-range selective transport of anions and cations in GOM causing crystallization on the macroscale. *Nanoscale Adv.* **3**, 353 (2021).
31. Qian, Y. et al. Boosting osmotic energy conversion of graphene oxide membranes via self-exfoliation behavior in nano-confinement spaces. *J. Am. Chem. Soc.* **144**, 13764–13772 (2022).
32. Chen, L. et al. Ion sieving in graphene oxide membranes via cationic control of interlayer spacing. *Nature* **550**, 380–383 (2017).
33. Fei, W., Xue, M., Qiu, H. & Guo, W. Heterogeneous graphene oxide membrane for rectified ion transport. *Nanoscale* **11**, 1313–1318 (2019).
34. Joshi, R. K. et al. Precise and ultrafast molecular sieving through graphene oxide membranes. *Science* **343**, 752–754 (2014).
35. Sun, P. et al. Electricity generation and local ion ordering induced by cation-controlled selective anion transportation through graphene oxide membranes. *2D Mater.* **1**, 034004 (2014).
36. Fontananova, E. et al. Effect of solution concentration and composition on the electrochemical properties of ion exchange membranes for energy conversion. *J. Power Sources* **340**, 282–293 (2017).
37. Tufa, R. A. et al. Potential of brackish water and brine for energy generation by salinity gradient power-reverse electrodialysis (SGP-RE). *RSC Adv.* **4**, 42617–42623 (2014).
38. Kingsbury, R. S., Flotron, S., Zhu, S., Call, D. F. & Coronell, O. Junction potentials bias measurements of ion exchange membrane permselectivity. *Environ. Sci. Technol.* **52**, 4929–4936 (2018).
39. Cho, Y. H. et al. Water and ion sorption, diffusion, and transport in graphene oxide membranes revisited. *J. Membr. Sci.* **544**, 425–435 (2017).
40. Yu, W., Yu, T., (Yet) & Graham, N. Development of a stable cation modified graphene oxide membrane for water treatment. *2D Mater.* **4**, 045006 (2017).
41. Kumar, P. et al. Novel radiation-induced properties of graphene and related materials. *Chem. Synth. Appl. Graphene Carbon Mater.* **213**, 1146–1163 (2012).
42. Yu, H. et al. Weak-reduction graphene oxide membrane for improving water purification performance. *J. Mater. Sci. Technol.* **39**, 106–112 (2020).
43. Schwenzer, B., Kaspar, T. C., Shin, Y. & Gotthold, D. W. Spectroscopic study of graphene oxide membranes exposed to ultraviolet light. *J. Phys. Chem. C* **120**, 12559–12567 (2016).
44. Ding, Y. H. et al. A green approach to the synthesis of rGO nanosheets under UV irradiation. *Nanotechnology* **22**, 215601 (2011).
45. Han, D.-D. et al. Bioinspired graphene actuators prepared by unilateral UV irradiation of graphene oxide papers. *Adv. Funct. Mater.* **25**, 4548–4557 (2015).
46. Yuan, S., Li, Y., Xia, Y., Selomulya, C. & Zhang, X. Stable cation-controlled reduced graphene oxide membranes for improved NaCl rejection. *J. Membr. Sci.* **621**, 118995 (2021).
47. Li, Y. et al. Thermally reduced nanoporous graphene oxide membrane for desalination. *Environ. Sci. Technol.* **53**, 8314–8323 (2019).
48. Li, Y. et al. Mild annealing reduced graphene oxide membrane for nanofiltration. *J. Membr. Sci.* **601**, 117900 (2020).
49. Ganguly, A., Sharma, S., Papakonstantinou, P. & Hamilton, J. Probing the thermal deoxygenation of graphene oxide using high-resolution in situ X-ray-based spectroscopies. *J. Phys. Chem. C* **115**, 17009–17019 (2011).
50. Shulga, Y. M., Shulga, N., Yu & Parkhomenko, Y. N. Carbon nanostructures reduced from graphite oxide as electrode materials for supercapacitors. *Mod. Electron. Mater.* **1**, 1–9 (2015).
51. Mao, Y. et al. Bola-amphiphile-imidazole embedded GO membrane with enhanced solvent dehydration properties. *J. Membr. Sci.* **595**, 117545 (2020).
52. Emiru, T. F. & Ayele, D. W. Controlled synthesis, characterization and reduction of graphene oxide: a convenient method for large scale production. *Egypt. J. Basic Appl. Sci.* **4**, 74–79 (2017).
53. Vanysek, P. *CRC Handbook of Chemistry and Physics* 93 edn (CRC Press, 1977).
54. Sun, P. et al. Realizing synchronous energy harvesting and ion separation with graphene oxide membranes. *Sci. Rep.* **4**, 5528 (2014).
55. Yang, H., Li, J. S. & Zeng, X. Correlation between molecular structure and interfacial properties of edge or basal plane modified graphene oxide. *ACS Appl Nano Mater.* **1**, 2763–2773 (2018).
56. Lerf, A., He, H., Forster, M. & Klinowski, J. Structure of graphite oxide revisited. *J. Phys. Chem. B* **102**, 4477–4482 (1998).
57. Han, Dong-Dong et al. Bioinspired graphene actuators prepared by unilateral UV of GO papers. *Adv. Funct. Mater.* **25**, 4548–4557 (2015).
58. Frindy, S. et al. Chitosan-graphene oxide films and CO₂-dried porous aerogel microspheres: interfacial interplay and stability. *Carbohydr. Polym.* **167**, 297–305 (2017).
59. Kingsbury, R. S. & Coronell, O. Modeling and validation of concentration dependence of ion exchange membrane permselectivity: significance of convection and Manning's counter-ion condensation theory.pdf. *J. Membr. Sci.* **620**, 118411 (2021).
60. Hernández-Luis, F., Rodríguez-Raposo, R. & Grandoso, D. Activity coefficients of NaBr in aqueous mixtures with high relative permittivity cosolvent: formamide + water at 298.15 K. *J. Chem. Eng. Data* **56**, 3940–3948 (2011).
61. Rodil, Eva & Vera, J. H. Individual activity coefficients of chloride ions in aqueous solutions of MgCl₂ CaCl₂ and BaCl₂ at 298.2K.pdf. *Fluid Phase Equilib.* **187–188**, 15–27 (2001).
62. Taghikhani, V., Modarress, H. & Vera, J. H. Individual anionic activity coefficients in aqueous electrolyte solutions of LiCl and LiBr. *Fluid Phase Equilib.* **166**, 67–77 (1999).
63. Ghalami-Chooabar, B. & Nosrati Fallahkar, T. Mean activity coefficients measurement of sodium chloride and thermodynamic modeling of sodium chloride and polysodium acrylate aqueous mixtures at T=(298.2 and 303.2)K. *Fluid Phase Equilib.* **378**, 51–59 (2014).
64. Amado, G., Eliseo & Blanco, L. H. Osmotic and activity coefficients of aqueous solutions of KCl at temperatures of 283.15, 288.15, 293.15 and 298.15K. A new isopiestic apparatus.pdf. *Fluid Phase Equilib.* **226**, 261–265 (2004).

65. Fontananova, E. et al. Probing membrane and interface properties in concentrated electrolyte solutions. *J. Memb. Sci.* **459**, 177–189 (2014).
66. Vermaas, D. A., Veerman, J., Saakes, M. & Nijmeijer, K. Influence of multivalent ions on renewable energy generation in reverse electrodialysis. *Energy Environ. Sci.* **7**, 1434 (2014).

ACKNOWLEDGEMENTS

This project has received funding from the European Union's Horizon 2020 research and innovation program within the project "intelligent Water Treatment Technologies for water preservation combined with simultaneous energy production and material recovery in energy-intensive industries—intelWATT" (Grant agreement No 958454).

The authors would like to acknowledge REDstack BV for the useful discussion about permselectivity and resistance measurements and Prof. Stefano Stassi (Politecnico di Torino) for the support during mechanical measurements.

AUTHOR CONTRIBUTIONS

A.A.-P., A.P., and A.L. designed the experiments and analyzed the data. M.L. pursued some characterization analyses. S.B. and I.V.F. carried out the preparation of the SPEEK polymer. Finally, E.F. offered support in the electrochemical characterization. All authors contributed to the final form of the manuscript.

COMPETING INTERESTS

The authors declare no competing interests.

ADDITIONAL INFORMATION

Supplementary information The online version contains supplementary material available at <https://doi.org/10.1038/s41699-023-00399-9>.

Correspondence and requests for materials should be addressed to Andrea Lamberti.

Reprints and permission information is available at <http://www.nature.com/reprints>

Publisher's note Springer Nature remains neutral with regard to jurisdictional claims in published maps and institutional affiliations.



Open Access This article is licensed under a Creative Commons Attribution 4.0 International License, which permits use, sharing, adaptation, distribution and reproduction in any medium or format, as long as you give appropriate credit to the original author(s) and the source, provide a link to the Creative Commons license, and indicate if changes were made. The images or other third party material in this article are included in the article's Creative Commons license, unless indicated otherwise in a credit line to the material. If material is not included in the article's Creative Commons license and your intended use is not permitted by statutory regulation or exceeds the permitted use, you will need to obtain permission directly from the copyright holder. To view a copy of this license, visit <http://creativecommons.org/licenses/by/4.0/>.

© The Author(s) 2023